Grain boundary-driven magnetism in aluminum nitride

Zhiming Shi, Hang Zang, Xiaobao Ma, et al.

View Online   Export Citation   CrossMark

ARTICLES YOU MAY BE INTERESTED IN

Physical origin of the endurance improvement for HfO_2-ZrO_2 superlattice ferroelectric film
Applied Physics Letters **121**, 242901 (2022); https://doi.org/10.1063/5.0127136

Implementation of electron restriction layer in n–AlGaN toward balanced carrier distribution in deep ultraviolet light-emitting-diodes
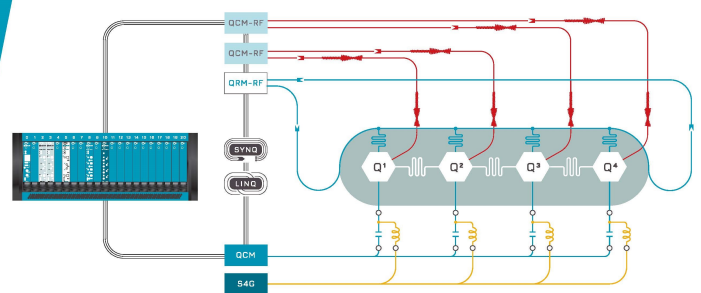Applied Physics Letters **121**, 241105 (2022); https://doi.org/10.1063/5.0131013

Charge to spin conversion in van der Waals metal $NbSe_2$
Applied Physics Letters **121**, 242404 (2022); https://doi.org/10.1063/5.0121577

Grain boundary-driven magnetism in aluminum nitride

Zhiming Shi,[1] (iD) Hang Zang,[1] Xiaobao Ma,[1,2] Yuxin Yang,[1,2] Ke Jiang,[1] Yang Chen,[1] (iD) Yuping Jia,[1]
Xiaojuan Sun,[1,a] (iD) and Dabing Li[1,2,a] (iD)

AFFILIATIONS

[1] State Key Laboratory of Luminescence and Applications, Changchun Institute of Optics, Fine Mechanics and Physics,
Chinese Academy of Sciences, Changchun 130033, China
[2] Center of Materials Science and Optoelectronics Engineering, University of Chinese Academy of Sciences, Beijing 100049, China

[a] Authors to whom correspondence should be addressed: sunxj@ciomp.ac.cn and lidb@ciomp.ac.cn

ABSTRACT

Introducing magnetism into III-nitrides to achieve diluted magnetic semiconductors (DMSs) is promising to broaden the applications of
III-nitrides. The most popular technique is doping transition metals; however, these structural imperfections are unstable due to significant
lattice incompatibility with the host. As a result, the fabrication of high-quality samples is quite difficult through the current growth techniques. Therefore, realizing intrinsic and robust magnetism in III-nitrides is quite desirable. Here, we adapted aluminum nitride as the example
to theoretically predict the stable magnetism driven by the ubiquitous grain boundaries (GBs). The magnetism strongly depends on GBs tilt
angles. These GBs cores contain homo-elemental bonds antiferromagnetically coupled at high tilt angles ($>16.7°$) due to the short coupling
distances. The T_c was as high as 293 K at the tilt angle of 32.2°. Importantly, the magnetism induced by GBs is robust regarding carrier
doping and strain, implying stable magnetism under working conditions. Our results provided a feasible and flexible approach to convert
III-nitride into a wide-gap DMS by engineering the topological GBs.

Published under an exclusive license by AIP Publishing. https://doi.org/10.1063/5.0132005

III-nitrides and their optoelectronic devices have attracted much
attention due to their outstanding physical and chemical properties,[1,2]
particularly in photoelectronic devices including light-emitting
diodes,[3,4] photodetectors,[5,6] and laser diodes.[7,8] Introducing magnetism into III-nitrides is promising to create functionalities beyond conventional III-nitrides since it enables simultaneous control of the
spin and charge.[9,10] Consequently, the rapid growth of research about
III-nitrides-based diluted magnetic semiconductors (DMSs) has
appeared.[11–15] According to the mean-field Zener model, the lighter
cation leads to weaker spin–orbital coupling and longer polarized carrier lifetime; therefore, GaN and AlN, in particular, are promising candidates to fabricate DMSs.[16,17]

The most popular technique to endow AlN with magnetism is
doping transition metals (TMs) to replace the Al site.[13,17–23] The density of functional theory (DFT) calculations predicted the feasibility of
TM doping.[17,18] The following experimental confirmations were
reported. Pan *et al.* incorporated Ni into AlN on a Si substrate by radio
frequency reactive sputtering, and the Curie temperature was beyond
300 K.[13] Endo and co-workers revealed the low-temperature ferromagnetism in $Al_{0.93}Cr_{0.07}N$ and $Al_{0.91}Mn_{0.09}N$ alloys with effective

magnetic moments of 0.51 μ_B/Cr 0.35 μ_B/Mn.[19] Han *et al.* realized
high saturation magnetization by Gd^+ ions implantation.[20] Xu's group
reported the room temperature ferromagnetism in Mg-doped AlN
nanowire and emphasized the effect of Al vacancy on the ferromagnetism.[23] Moreover, the point defects can introduce magnetism in
AlN.[24–28] The nitrogen-vacancy induced sizable ferromagnetic (FM)
coupling in 2H-AlN, and the magnetism can be tuned by controlling
the concentration of defects.[24] While the magnetic signals can be
experimentally detected in certain AlN samples, these systems still
showed limitations. The magnetism in AlN originated from the TM
adatoms or vacancies; however, these structural imperfections are not
stable due to considerable lattice incompatibility between the TM adatoms and the Al atoms. It is hard to obtain high-quality samples
through the current growth techniques. Several works reported that
ferromagnetism strongly depended on the aggregation of TM adatoms,[29,30] which was too hard to control during the growth. In addition, the structural defects can be readily healed by the local
reconstruction or diffusion through annealing,[31,32] leading to the magnetism being destroyed. Therefore, the realization of intrinsic and
robust magnetism in AlN is quite desirable.

Grain boundaries (GBs), a type of topological defect, are ubiquitous in III-nitrides because of the obvious mismatch between substrates and epilayers induced by the most frequently used heteroepitaxy technique.[33–35] Different from the TM-dopants, the topological GBs are quite robust. Therefore, they are hard to be recovered through local atomic reconstruction. Meanwhile, the GBs can also break the intrinsic electronic occupancy state of perfect structures and perhaps produce magnetism. Here, we reported by the first-principles calculations that GBs in AlN can produce substantial magnetic moments, due to the partial occupancy induced by the homo-elemental bonds. The 5|7 cores are identified to be the stable configuration of GBs and behave as an antiferromagnetic (AFM) coupling at big tilt angles. The magnitude of magnetic moments strongly depends on the tilt angles and exhibits great robustness regarding strain and carrier doping. The half-metallic property can be realized in AlN. Our results reveal an interesting interaction between GBs and spin freedom, opening a pathway for exploring spintronics in wide-gap III-nitrides.

In this work, we used wurtzite AlN supercells. The projector-augmented wave (PAW) method was adopted by employing the Vienna *Ab initio* Simulation Package (VASP).[36] Spin-polarized was included. The exchange–correlation interaction of electrons was described by using the Perdew–Burke–Ernzerhof (PBE) functional.[37] The 500 eV of plane wave energy cutoff was used; Γ-center k-mesh was sampled in the first Brillouin zone, 0.04 $2\pi/\text{Å}$ for structural relaxation and 0.02 $2\pi/\text{Å}$ for spin-resolved self-consistent calculations, respectively. The convergence thresholds of electronic iteration and force were set to 10^{-4} eV and 0.02 eV/Å, respectively. Both lattice parameters and atomic positions were included in structural relaxation.

The VASPKIT[38] and VESTA[39] codes were used for data post-processing and structural visualization.

The GBs were along the c-axis, consistent with the direction of growth. They were created by removing atomic ribbons along the armchair direction and seamlessly reconnecting residual dangling bonds yielding a dislocation core to minimize the redundant strain. A superlattice vector $\mathbf{R} = m\mathbf{a_1} + n\mathbf{a_2}$ was defined, where $\mathbf{a_1}$ and $\mathbf{a_2}$ were the in-plane primitive vectors of AlN, to build the GBs with different tilt angles (2θ) by varying m and n (m, n), as shown in Fig. 1(a). Following this description, the GB with $2\theta = 27.8°$ can be represented as $\mathbf{R} = 3\mathbf{a_1} + 1\mathbf{a_2}$, which is marked as (3, 1). The tilt angles were in the range of $0° < 2\theta < 60°$ because of the hexagonal symmetry of the wurtzite AlN, so we adapted six different 2θ, including 7.8° (5, 4), 10.2° (4, 3), 16.4° (5, 3), 27.8° (3, 1), 32.2° (5, 2), and 42.2° (5, 1), in the following discussion. The optimized structures with spin-resolved charge densities were shown in Fig. 1(b). Two decisive factors that govern the formation energy of GBs are strain and bonding properties. The strain energy (E_s) induced by GBs can be reflected by Burges vector $|\mathbf{b}|$ ($E_s \propto |\mathbf{b}|^2$); this is lowest for 5|7 core according to our calculations, particularly for low tilt angle GBs, as shown in Fig. 1(b).

The calculated formation energies (E_{form}) confirmed our analysis. As shown in Fig. 2(a) (red line), the E_{form} increased with the tilt angle, implying the formation of high-tilt-angle GB required a high-thermal growth condition, for example, high temperature or an external light field. Because the Burges vector $|\mathbf{b}|$ became larger by increasing the tilt angle, the big strain energy result in the increase in E_{form}. The tilt-dependence E_{form} was mainly governed by two factors at the atomic scale: (1) The bonding energies (or stability) of the Al–N bonds
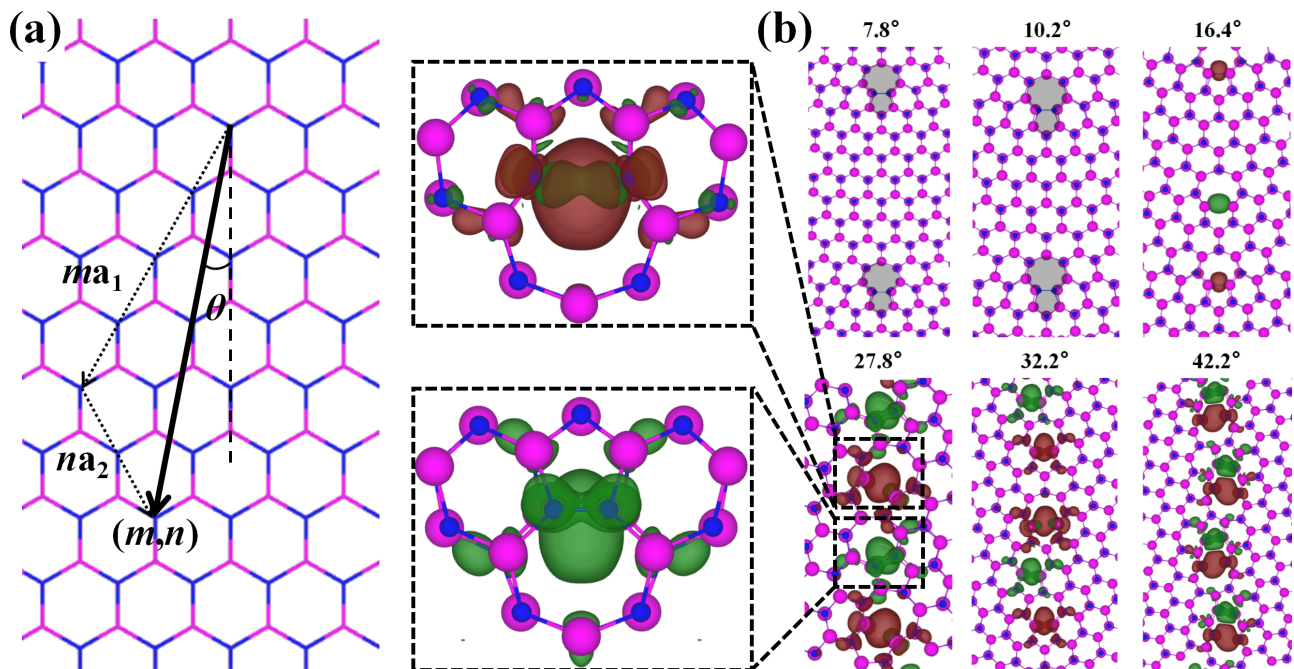
FIG. 1. Structures of grain boundary in wurtzite AlN. (a) Structural diagram of symmetric GB with different tilt angle 2θ. (b) Atomic structural and spin-resolved charge density of GBs with different tilt angles. Each repeat unit includes GB 5|7 cores with Al–Al and N–N homo-elemental bonds. The 5|7 cores are highlighted by gray shadows. Red and green colors denote positive and negative values of the magnetization density, respectively. Loose (up) and tight (down) bonding 5|7 cores of $2\theta = 27.8°$ GB were picked out.
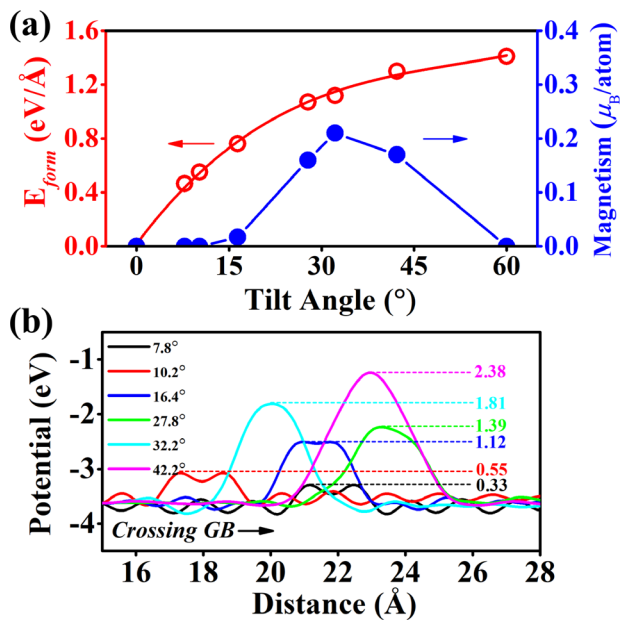
FIG. 2. Tilt-dependent properties of GBs in AlN. (a) Magnetism per atom (blue line) and formation energies (E_{form}, red line) as the function of tilt angle. Magnetic moments are the absolute values obtained from GBs with AFM order. (b) The in-plane average electrostatic potential barriers as the function of tilt angles, and the x-axis is the distance from the edge of the supercell along the direction vertical to the GB.

TABLE I. The energies of different magnetic states for each GB.

	E_{NM} (eV)	E_{AFM} (eV)	$E_{NM} - E_{AFM}$ (eV)	T_c (K)
7.8° (5, 4)	−2784.552	N/A		
10.2° (4, 3)	−1896.074	N/A		
16.4° (5, 3)	−2289.880	−2289.876	−0.003	12
27.8° (3, 1)	−2213.338	−2213.406	0.068	135
32.2° (5, 2)	−1200.236	−1200.332	0.111	293
42.2° (5, 1)	−2049.758	−2049.834	0.076	131
60.0° (5, 0)	−1477.629	N/A		

(AFM) states for each structure, and the results were listed in Table I. The 7.8° and 10.2° structures exhibited NM states, no spin-polarization was obtained after optimization. For the 16.4°, we can find the NM state was more stable than the magnetic state by just 0.003 eV (the initial FM order optimized to the AFM order after electronic self-consistent for all magnetic systems). Above 16.4°, the GBs showed AFM ground states with different spin states located at neighboring 5|7 cores. With increasing the tilt angle, the energy deviation between NM and AFM states increased and reached the maximum at 32.2°, then decayed to the NM state at 60°. The tilt-dependent magnetism can be observed in Fig. 2(a) (blue line). The magnetic moment per atom exhibited a volcano shape with increasing the tilt angle and reached the maximum of 0.21 μ_B/atom (0.42 μ_B per 5|7 core) at 32.2°. The GBs not only induced magnetism but also formed potential barriers in the materials; meanwhile, the barriers monotonously went up from 0.33 to 2.38 eV with the tilt angle [Fig. 2(b)], implying the carriers were restricted by GBs. The calculated Curie Temperatures (T_c) by mean-field theory[16] were listed in Table I. The T_c of 32.2° GB is as high as 293 K, indicating room-temperature magnetism.

To reveal the origin of the magnetic moment for GBs, the spin-polarized density of states (DOS) was calculated, and the GBs-relative states were spatially projected as shown in Fig. 3. The 10.2° [Fig. 3(a)] and 32.2° [Fig. 3(b)] GBs were adapted as examples. The states related to the GBs were spatially projected onto the atoms. The states of the bulk part were shaded by gray shallow. The GBs induced two states in the bandgap for the 10.2° structure, the δ and $\delta*$ states separated by the Fermi level. The occupied δ state originated from the N–N homo-elemental bonding state, while the unoccupied δ^* state showed a corresponding antibonding character, as shown in Fig. 3(a). The spin polarization cannot be observed due to the full occupation character of these states for the 10.2° structure. While the tilt angle increased, the 5|7 cores became closer to each other, and the energy split occurred. As shown in Fig. 3(b), the δ state in the 32.2° structure broadened in both spin channels and cross the Fermi level due to the adjacent 5|7 cores coupling. The N–N homo-elemental in one 5|7 core was broken to form a loose bond, but still tightly bonded in another. It can be explained by the Stoner model, which is the electronic states spontaneously triggered spin splitting when the δ state crossed the Fermi level, that echoed the spatial distribution of the N–N δ state. On the other hand, the $\delta*$ states were still localized. This effect was gradually enhanced by increasing the tilt angles since the coupling was strengthened due to the reduced distance between adjacent 5|7 cores. The structures of 27.8°, 32.2°, and 42.2° exhibited similar magnetic moments because they possessed the nearest 5|7 core pairs.

surrounding the 5|7 cores were reduced. Both Al and N atoms tetrahedrally bonded in intrinsic AlN but distorted due to the formation of the 5|7 cores. (2) Unavoidably, the energetic unfavorable homo-elemental bonds (including the Al–Al and N–N bonds) were formed, whose energies were much higher than the Al–N bonds. At a small tilt angle, such as 7.8° and 10.2° shown in Fig. 1(b), the homo-elemental bonds formed in each 5|7 core to stabilize the dangling bonds, because the interaction between the adjacent 5|7 cores was weak at a small tilt angle. When the tilt angle increased, the distance between the adjacent 5|7 cores was shortened and the density of 5|7 cores increased, the local stress became serious due to the squeezed 5|7 cores. As a result, the homo-elemental bond in one 5|7 core was broken to form loose bonding, while keeping tight bonding in the neighbor 5|7 core, as shown in the zoom-in of Fig. 1(b). We also considered the 4|8 cores, without homo-elemental bonds but more serious strain than 5|7 cores, only the $2\theta = 60°$ GB showed 4|8 ground structure (as shown in Fig. S1), while the 4|8 cores collapsed during structural relaxations for other tilt angles GBs due to the serious strain. The crystallographic orientation is identified at the nucleation stage; moreover, the tilt angle of GBs is hard to be tuned once it forms during heteroepitaxy due to the strong covalent bonding between the epilayer and substrate. Therefore, two approaches may be applied to obtain GBs with desired tilt angle. First, the growth temperature should be increased to compensate for the excessive E_{form} during the nucleation stage. Second, we can weaken the interaction between the epilayer and substrate to enhance the tunability of the tilt angle. The recent development of the van der Waals epitaxy provided a promising approach to this aim.[40–44]
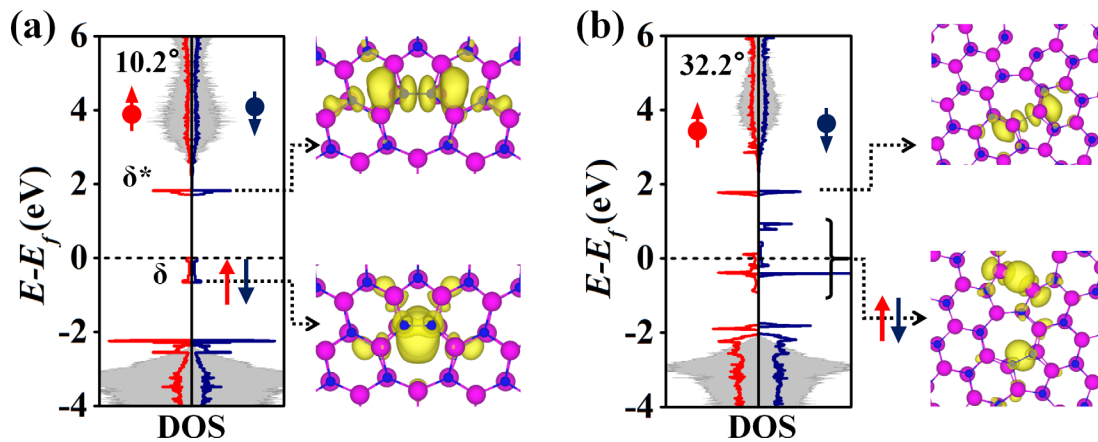
To determine the ground state, we compared the energies of nonmagnetic (NM), ferromagnetic (FM), and antiferromagnetic

FIG. 3. Electronic structure analyses of dislocation in AlN. Spin-polarized density of states (DOS) and energy-level-resolved isosurface distributions of partial charge density for (a) $2\theta = 10.2°$ and (b) $2\theta = 32.2°$ AlN GBs. The solid lines are the projected DOS onto GBs, and the gray-shaded regions are the DOS onto bulk part.

The electronic states coupling between the adjacent 5|7 cores became serious with GBs tilt angles. It not only enhanced the coupling but also broadened the dispersive defect states. If this effect on dispersion is unequal in the different spin channels, one channel crosses the Fermi level but another one does not, and the half-metallic property is obtained. The spin-polarized density of states for $2\theta = 16.4°$, 27.8°, and 42.2° structures was presented in Fig. 4. They opened sizable gaps of 0.28 and 1.06 eV in the spin-down channels and formed metallic spin-up channels for $2\theta = 16.4°$ and 42.2° GBs, due to the δ state of N–N bond splitting was stronger than the state broadening, as shown in Figs. 4(a) and 4(c). At $2\theta = 27.8°$ [Fig. 4(b)], the GBs supported an insulating (the gap is 0.90 eV) spin-up channel and a metallic spin-down channel. At $2\theta = 32.2°$ [Fig. 3(b)], both spin channels were metallic. At low tilt angles [$2\theta = 7.8°$ and 9.2°, in Figs. 3(a) and S2], the GBs were nonmagnetic semiconductors in this work, since the weak band dispersion cannot metalize any spin channel. At $2\theta = 60°$, the 4|8 core was stable and nonmagnetic semiconducting, as shown in Fig. S1. These results support the feasibility of tailoring the spin-dependent transport by engineering GBs in III-nitrides.

The robustness of the magnetism is necessary for the reliability of devices. Magnetism is sensitive to carrier doping that is always affected by external gating or intrinsic doping in practical applications. Here, we investigated the magnetism for different carrier doping levels by calculating the magnetic moments as a function of charge states (add/reduce electrons under a jellium background). The $2\theta = 27.8°$ GB was adapted as the example. As present in Fig. 5(a), the magnetism has remained after both hole and electron doping. The doping level was in the range from -2 to 2 e/cell, whose carrier density was close to the working condition (the magnitude is about $10^{20}\,\text{cm}^{-3}$). The effect of magnetism for hole doping is more significant than that for electron doping. The minimum magnetism (0.07 μ_B/atom) appeared at the hole doping level of 1.6 e/cell, and the maximum (0.28 μ_B/atom) was at the hole doping level of 0.4 e/cell. On the other hand, the magnetic moment just fluctuated in the range of 0.15–0.19 μ_B/atom under electron doping as high as 2.0 e/cell, indicating the magnetism induced by GBs showed good robustness in respect of electron doping. Moreover, the AlN underwent strain due to the significant lattice mismatch during hetero-epitaxy growth. We also studied whether the strain along different crystallographic orientations will affect the magnetism, and the results were displayed in Fig. 5(b). The magnetic moments just fluctuated from 0.20 to 0.26 μ_B/atom when the strain varied from -5% to 5% whatever the directions. Therefore, the magnetism
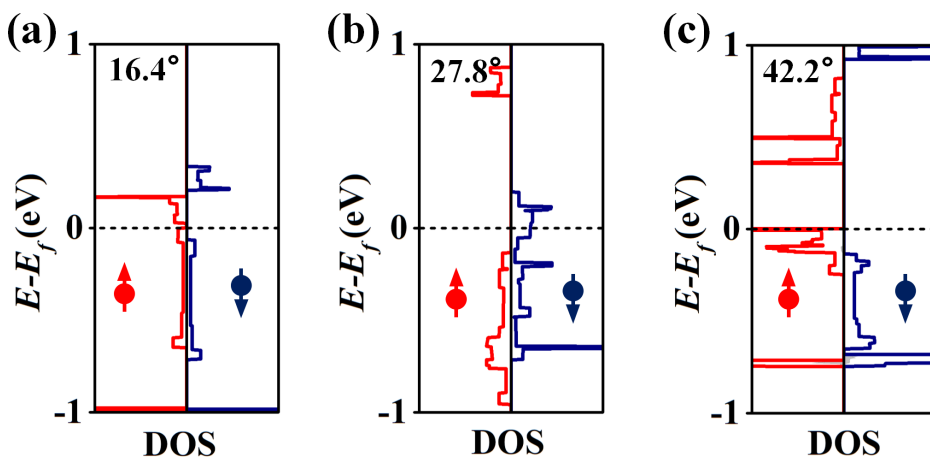
FIG. 4. Spin-polarized DOS of (a) $2\theta = 16.4°$, (b) $2\theta = 27.8°$, and (c) $2\theta = 42.2°$ GBs. The color stipulations are the same as in Fig. 3.
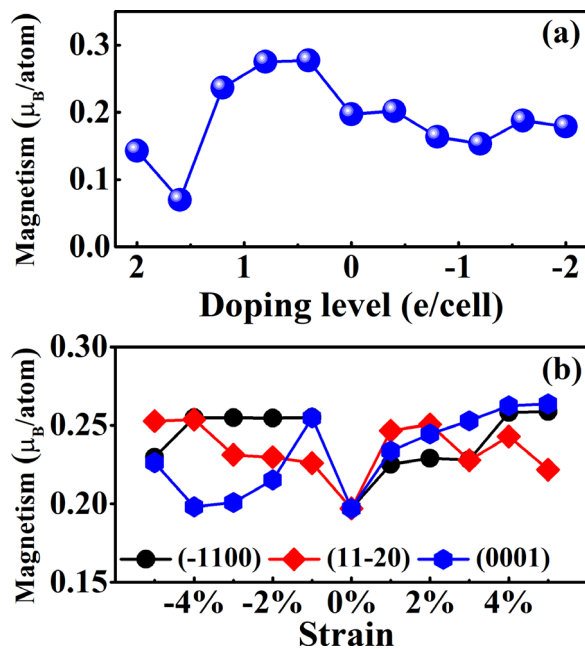
FIG. 5. The robustness of the magnetism for GB with $2\theta = 27.8°$. The magnetism as the function of (a) carrier doping level and (b) strain along different directions. Due to the different in-plane crystallographic orientations of the grains, there is about $13.9°$ divergence along (-1100) and $(11\text{-}20)$ for the calculated strain.

induced by the GBs in AlN also showed excellent robustness in respect of strain.

In this work, a comprehensive first-principles study on the magnetism driven by GBs was revealed in AlN. The magnetism showed an angle dependence and good robustness. The magnetic moment associated with localized defect states centered on N–N homo-elemental bonding state within the bandgap of AlN. GBs show antiferromagnetic spin ordering on the adjacent 5|7 cores, which form a metallic channel in AlN. Half-metal or metal was observed at the tilt angle exceeding $16.4°$. At $2\theta = 60°$, GBs composed of 4|8 cores were energetically favorable and were nonmagnetic semiconductors due to the lack of homo-elemental bonds. Magnetism showed great robustness regarding doping level and strain. Grain boundaries are unavoidable in III-nitrides due to the hetero-epitaxy fabrication. The coupling of spin-polarization and GBs pave a feasible way to realize DMS based on III-nitrides through GBs engineering.

See the supplementary material for the atomic structure of 4|8 GB at $2\theta = 60°$, and the complete density of states (DOS) for all studied GBs.

AUTHOR DECLARATIONS
Conflict of Interest

The authors have no conflicts to disclose.

Author Contributions

Zhiming Shi: Conceptualization (lead); Writing – original draft (lead); Writing – review & editing (lead). **Hang Zang:** Data curation (supporting); Writing – review & editing (supporting). **Xiaobao Ma:** Data curation (supporting); Writing – review & editing (supporting). **Yuxin Yang:** Data curation (supporting); Writing – review & editing (supporting). **Ke Jiang:** Writing – review & editing (supporting). **Yang Chen:** Writing – review & editing (supporting). **Yuping Jia:** Writing – review & editing (supporting). **Xiaojuan Sun:** Conceptualization (equal); Supervision (equal); Writing – original draft (equal); Writing – review & editing (equal). **Dabing Li:** Conceptualization (lead); Resources (lead); Supervision (lead); Writing – review & editing (equal).

DATA AVAILABILITY

The data that support the findings of this study are available from the corresponding author upon reasonable request.

REFERENCES

[1]S. N. Mohammad and H. Morkoç, Prog. Quantum Electron. **20**, 361–525 (1996).

[2]D. Li, K. Jiang, X. Sun, and C. Guo, Adv. Opt. Photonics **10**, 43–110 (2018).

[3]S. Nakamura, T. Mukai, and M. Senoh, Appl. Phys. Lett. **64**, 1687–1689 (1994).

[4]Y. Sun, K. Zhou, M. Feng, Z. Li, Y. Zhou, Q. Sun, J. Liu, L. Zhang, D. Li, and X. Sun, Light: Sci. Appl. **7**, 1–7 (2018).

[5]D. Li, X. Sun, H. Song, Z. Li, Y. Chen, H. Jiang, and G. Miao, Adv. Mater. **24**, 845–849 (2012).

[6]D. Li, X. Sun, H. Song, Z. Li, Y. Chen, G. Miao, and H. Jiang, Appl. Phys. Lett. **98**, 011108 (2011).

[7]Z. Li, J. Liu, M. Feng, K. Zhou, S. Zhang, H. Wang, D. Li, L. Zhang, D. Zhao, and D. Jiang, Appl. Phys. Lett. **103**, 152109 (2013).

[8]Y. Zhang, T.-T. Kao, J. Liu, Z. Lochner, S.-S. Kim, J.-H. Ryou, R. D. Dupuis, and S.-C. Shen, J. Appl. Phys. **109**, 083115 (2011).

[9]H. Ohno, Science **281**, 951–956 (1998).

[10]I. Žutić, J. Fabian, and S. D. Sarma, Rev. Mod. Phys. **76**, 323 (2004).

[11]R. Wu, G. Peng, L. Liu, Y. Feng, Z. Huang, and Q. Wu, Appl. Phys. Lett. **89**, 062505 (2006).

[12]B. Amin, S. Arif, I. Ahmad, M. Maqbool, R. Ahmad, S. Goumri-Said, and K. Prisbrey, J. Electron. Mater. **40**, 1428–1436 (2011).

[13]D. Pan, J. Jian, A. Ablat, J. Li, Y. Sun, and R. Wu, J. Appl. Phys. **112**, 053911 (2012).

[14]Y. K. Zhou and H. Asahi, *Molecular Beam Epitaxy: Materials and Applications for Electronics and Optoelectronics* (Wiley, 2019), pp. 299–313.

[15]C. Timm, *Spintronics Handbook: Spin Transport and Magnetism*, 2nd ed. (CRC Press, 2019), pp. 371–411.

[16]T. Dietl, H. Ohno, F. Matsukura, J. Cibert, and D. Ferrand, Science **287**, 1019–1022 (2000).

[17]V. Litvinov and V. Dugaev, Phys. Rev. Lett. **86**, 5593 (2001).

[18]X. Cui, D. Fernandez-Hevia, B. Delley, A. Freeman, and C. Stampfl, J. Appl. Phys. **101**, 103917 (2007).

[19]Y. Endo, T. Sato, A. Takita, Y. Kawamura, and M. Yamamoto, IEEE Trans. Magn. **41**, 2718–2720 (2005).

[20]S. Y. Han, J. Hite, G. Thaler, R. Frazier, C. Abernathy, S. Pearton, H. Choi, W. Lee, Y. Park, and J. Zavada, Appl. Phys. Lett. **88**, 042102 (2006).

[21]L.-J. Shi, L.-F. Zhu, Y.-H. Zhao, and B.-G. Liu, Phys. Rev. B **78**, 195206 (2008).

[22]P. Dev, Y. Xue, and P. Zhang, Phys. Rev. Lett. **100**, 117204 (2008).

[23]Y. Xu, B. Yao, D. Liu, W. Lei, P. Zhu, Q. Cui, and G. Zou, CrystEngComm **15**, 3271–3274 (2013).

[24]Y. Liu, L. Jiang, G. Wang, S. Zuo, W. Wang, and X. Chen, Appl. Phys. Lett. **100**, 122401 (2012).

[25]D. Pan, J. Jian, Y. Sun, and R. Wu, J. Alloys Compd. **519**, 41–46 (2012).

[26]Y. Gao, D. Sun, X. Jiang, and J. Zhao, J. Appl. Phys. **125**, 215705 (2019).

[27]Z. Shi, Z. Qi, H. Zang, K. Jiang, Y. Chen, Y. Jia, T. Wu, S. Zhang, X. Sun, and D. Li, ACS Appl. Mater. Interfaces **13**, 37380–37387 (2021).

[28]H. Zang, X. Sun, K. Jiang, Y. Chen, S. Zhang, J. Ben, Y. Jia, T. Wu, Z. Shi, and D. Li, Adv. Sci. **8**, 2100100 (2021).

[29]S. Yang, A. Pakhomov, S. Hung, and C. Wong, Appl. Phys. Lett. **81**, 2418–2420 (2002).

[30]S. Y. Wu, S. Liu, L. Gu, R. Singh, L. Budd, M. Van Schilfgaarde, M. McCartney, D. J. Smith, and N. Newman, Appl. Phys. Lett. **82**, 3047–3049 (2003).

[31]C. Kai, H. Zang, J. Ben, K. Jiang, Z. Shi, Y. Jia, X. Cao, W. Lü, X. Sun, and D. Li, J. Lumin. **235**, 118032 (2021).

[32]A. Uedono, K. Shojiki, K. Uesugi, S. F. Chichibu, S. Ishibashi, M. Dickmann, W. Egger, C. Hugenschmidt, and H. Miyake, J. Appl. Phys. **128**, 085704 (2020).

[33]D. A. Neumayer and J. G. Ekerdt, Chem. Mater. **8**, 9–25 (1996).

[34]V. Hrkac, A. Kobler, S. Marauska, A. Petraru, U. Schürmann, V. S. Kiran Chakravadhanula, V. Duppel, H. Kohlstedt, B. Wagner, and B. V. Lotsch, J. Appl. Phys. **117**, 014301 (2015).

[35]S. Yoon, H. Yoo, S.-H. Kang, M. Kim, and Y.-K. Kwon, Sci. Rep. **8**, 1–6 (2018).

[36]G. Kresse and D. Joubert, Phys. Rev. B **59**, 1758 (1999).

[37]J. P. Perdew, K. Burke, and M. Ernzerhof, Phys. Rev. Lett. **77**, 3865 (1996).

[38]V. Wang, N. Xu, J. C. Liu, G. Tang, and W. T. Geng, Comput. Phys. Commun. **267**, 108033 (2021).

[39]K. Momma and F. Izumi, J. Appl. Crystallogr. **44**, 1272–1276 (2011).

[40]L. Zhang, X. Li, Y. Shao, J. Yu, Y. Wu, X. Hao, Z. Yin, Y. Dai, Y. Tian, and Q. Huo, ACS Appl. Mater. Interfaces **7**, 4504–4510 (2015).

[41]Y. Qi, Y. Wang, Z. Pang, Z. Dou, T. Wei, P. Gao, S. Zhang, X. Xu, Z. Chang, and B. Deng, J. Am. Chem. Soc. **140**, 11935–11941 (2018).

[42]Z. Chen, Z. Zhang, Z. Dou, T. Wei, Z. Liu, Y. Qi, H. Ci, Y. Wang, Y. Li, and H. Chang, Adv. Mater. **30**, 1801608 (2018).

[43]Z. Shi, X. Sun, Y. Jia, X. Liu, S. Zhang, Z. Qi, and D. Li, Sci. China Phys. Mech. Astron. **62**, 1–7 (2019).

[44]Y. Chen, Z. Shi, S. Zhang, J. Ben, K. Jiang, H. Zang, Y. Jia, W. Lü, D. Li, and X. Sun, Adv. Electron. Mater. **8**, 2100759 (2022).